**Metabolic and imaging phenotypes associated with *RB1* loss in castrate resistant prostate cancer**

*Fahim Ahmad[1, 2, 3], *Margaret White[1,3], Kazutoshi Yamamoto[2], Daniel R. Crooks[4,5], Supreet Agarwal[3], Ye Yang[4,5], Brian Capaldo[3], Sonam Raj[3], Aian Neil Alilin[3], Anita Ton[1], Stephen Adler[6], Jurgen Seidel[1], Colleen Olkowski[1], Murali Krishna Cherukuri[2], Peter L Choyke[1], **Kathleen Kelly[3], and **Jeffery R. Brender[1,2]

1. Molecular Imaging Branch, NCI/NIH, Bethesda, MD-20892
2. Radiation Biology Branch, NCI/NIH, Bethesda, MD-20892
3. Laboratory of Genitourinary Cancer Pathogenesis, NCI/NIH, Bethesda, MD-20892
4. Urologic Oncology Branch, NCI, NIH, Bethesda, MD-20892
5. Clinical Cancer Metabolism Facility, NCI, NIH, Bethesda, MD-20892
6. Clinical Research Directorate, Frederick National Laboratory for Cancer Research. Frederick MD-21701

***These authors contributed equally**
****These authors contributed equally**

**Abstract**

Advanced prostate cancer is treated with androgen receptor (AR) signaling inhibitors, which are initially effective, but the majority of patients eventually develop resistance and progress to castration resistant prostate cancer (CRPC). Loss of *RB1* in CRPC tumors is correlated with rapid progression and poor patient survival, and in combination with *TP53* loss, predisposes to the development of transitional neuroendocrine prostate cancer (NEPC). Although progressing CRPC is clinically associated with higher [$^{18}$F]DG-PET $SUV_{max}$ values, it is unknown whether inactivation of *RB1* and/or *TP53* is a driver of increased glucose import. To study this, we used a cohort of PDX-derived CRPC organoids and observed that [$^{18}$F]DG uptake is higher in AR positive adenocarcinoma (ARPC) compared with NEPC and was not associated with genotype, including *RB1* status. In two ARPC models, experimental loss of RB1 increased glycolysis and oxygen consumption. While these metabolic changes were not detected in vitro or in vivo by [$^{18}$F]DG-PET, $^{13}$C-hyperpolarized magnetic resonance spectroscopy showed significant differences in lactate dehydrogenase flux upon loss of *RB1*. Loss of TP53 and RB1 created a new phenotype where glucose was diverted to the pentose phosphate pathway and into glycogen synthesis. These data demonstrate an increased glycolytic phenotype associated with *RB1* loss in ARPC unlinked to glucose uptake and suggest that the tumor microenvironment may play a major role in determining levels of [$^{18}$F]DG uptake in vivo.

## Introduction:

Oncogenic transformation and progression is often associated with metabolic reprogramming and this association can be exploited for molecular imaging, most notably with FDG-PET. From a molecular imaging perspective, prostate cancer is of great interest due to the extent of metabolic reprogramming and the unusual metabolism of the prostate. Normal epithelial cells in the prostate are characterized by high levels of aerobic glycolysis and low levels of oxidative metabolism as a result of TCA cycle truncation secondary to zinc inhibition of ACOC2 and citrate exportation to seminal fluid (*1,2*). Primary prostate cancer, which is almost always androgen receptor (AR) positive adenocarcinoma (ARPC), demonstrates an increased glycolytic phenotype with progression (*3*). This is consistent with several experimental studies demonstrating AR stimulated expression of multiple glycolytic proteins such as GLUT1, HK2, and PFK (*4,5*). In addition, a form of glycolytic flux dependent upon enhanced lactate secretion is associated with increased progression in primary prostate cancer and can be measured by hyperpolarized magnetic imaging (HP-MRI) (*6*).

Aggressive and/or recurrent prostate cancer is treated by inhibiting AR signaling, a pathway required by most tumor cells for growth and viability (*7*). Although treatment is usually initially efficacious, resistance to AR inhibition almost always develops as castrate resistant prostate cancer (CRPC). Most CRPC circumvents AR pathway inhibition through upregulating AR signaling either directly or indirectly, but about 15-20% of CRPC patients lose dependence upon AR signaling (*7,8*). While metabolic differences in individual tumors likely contribute to the efficacy of some cancer treatments, CRPC is highly heterogeneous (*9,10*), and the range of metabolic reprogramming as well as association with specific phenotypic and genotypic variations are unknown.

Analysis of recurrent CRPC genomic alterations relative to clinical outcome has identified *RB1* homozygous deletion, occurring in about 10% of CRPC, as singularly associated with poor survival (*11*). Prostate cancers with histological small cell neuroendocrine differentiation ($\leq$5%) typically have homozygous alterations in *RB1* in combination with *TP53*, as well as loss of AR expression (*12,13*). Adenocarcinomas (ARPC) with *RB1/TP53* alterations maintain AR signaling but demonstrate changes in proliferation and DNA repair pathways (*14*). The transition to NEPC occurs in ARPC via AR loss-associated acquisition of plasticity and subsequent differentiation along a neuroendocrine lineage (*15*). Although neither necessary nor sufficient, the loss of *RB1* is highly predisposing toward a NEPC transition, and therefore, identifying *RB1* loss in CRPC has implications for treatment choices and monitoring (*11*).

Classically, *RB1* acts as a tumor suppressor, although the effect of *RB1* loss is species and context dependent. One mechanism of *RB1* suppression is in preventing cell cycle progression by limiting the transcription of cell cycle genes via regulation of the E2F family of transcription factors. However, the most significantly upregulated pathways after *RB1* loss in the LNCaP C42B CRPC model, but not the parental hormone-sensitive LNCaP model, are related to metabolism (*16*) suggesting that inactivation of *RB1* may generate metabolic reprogramming that is influenced by progression to CRPC. Inactivation of RB1 in the LNCaP C42B CRPC model leads to an upregulation of genes associated with lipid and amino acid metabolism as well as glutathione

biosynthesis, transcriptomic changes that are enriched in *RB1* deficient patient samples (*16*).

Prostate cancer modeling historically has been hampered by a lack of tractable models reflective of the heterogeneity observed in patient CRPC cases. Several diverse PDX cohorts have been developed (*17*), but the ability to analyze metabolic and biochemical parameters are limited both by practicality and tumor purity in vivo. Thus, several prostate cancer-related metabolic studies have been based on limited tumor cell lines or from transcriptomic analyses of tumor samples, which are composed of mixtures of tumor and microenvironmental cellular components. We recently described the utility of PDX-derived organoids for in vitro analyses (*18*), and here we make use of an extensive cohort of clinically heterogeneous organoids to investigate $^{18}$FDG uptake and conversion of pyruvate to lactate on hyperpolarized MRI (HP-MRI) relative to established CRPC phenotypes and genotypes. From a clinical perspective, NEPC and aggressive CRPC metastases are characterized by an increase in FDG uptake seen in $^{18}$FDG-PET, which provides a convenient way of monitoring the disease and treatment response. However, we show here that patient-derived NEPC organoids composed exclusively of tumor cells demonstrated relatively low levels of autonomous FDG uptake, lower than many ARPCs exhibit in humans. Because *RB1* deficiency predicts poor survival and increased transformation to a NE phenotype, we further investigated the metabolic imaging modalities that monitor changes in metabolism in AR+ CRPC following *RB1* loss. *RB1* loss was associated with increased glycolysis, which was reflected in increased pyruvate to lactate flux in HP-MRI but not FDG uptake. This study characterizes the effect of RB1 and TP53 deletion on metabolic imaging in both ARPC and CRPC, and further identifies relative changes associated with *RB1* depletion in ARPC. Overall, our data do not support the hypothesis that NEPC tumor cells are responsible for increased FDG uptake observed clinically, but alternatively, such uptake likely occurs in non-malignant cells in the microenvironment which are metabolically activated by NEPC tumor biology.

## Results:

### NEPC cannot be conclusively distinguished from adenocarcinoma by $^{18}$FDG uptake alone in *in vitro* models

To broadly characterize $^{18}$FDG uptake in an extensive cohort of CRPC organoids relative to prostate cancer phenotype and genotype, we measured $^{18}$FDG uptake over 120 minutes in PDX-derived ARPC and NEPC organoids (n=18), patient biopsy-derived ARPC organoids (n=2), and ARPC cell lines (n=3). Figure 1A shows the percentage of $^{18}$FDG uptake normalized to the number of live cells for each model. Although the final $^{18}$FDG uptake values showed variation among the biological replicates, we observed at the final time point a clear separation between models with high and low $^{18}$FDG uptake, with a separation line occurring around 6% uptake (see Figs. 1A and S1A). While the distinction between high and low $^{18}$FDG uptake groups is evident, the correlation between $^{18}$FDG uptake and phenotype is not as straightforward. On average, adenocarcinoma (ARPC) models exhibited higher $^{18}$FDG uptake compared to NEPC models (8.1 ± 1.5% vs. 4.7 ± 2.1% SEM). With the exception of the LuCaP 145.1 organoids, all NEPC models fell into the low $^{18}$FDG uptake group. By contrast, adenocarcinoma models were almost equally distributed between the high and low

$^{18}$FDG uptake groups. Therefore, it is not possible to definitively distinguish lineage in organoid cultures based solely on $^{18}$FDG uptake.

### PSMA protein levels do not correlate with prostate cancer phenotype or $^{18}$FDG uptake in *in vitro* models

$^{18}$FDG imaging is not the only molecular imaging technique used for prostate cancer staging. PSMA targeted imaging is increasingly used in the clinic, thus, we compared *FOLH1* RNA levels, an excellent surrogate for PSMA protein levels, to $^{18}$FDG uptake in each model (Fig. 1B). As with $^{18}$FDG, there was a clear separation between high and low *FOLH1* groups. As expected from previous preclinical studies, ARPC models generally showed high *FOLH1* levels and *RB1* null models, including NEPC models, demonstrated markedly lower levels of FDG uptake, although there were two exceptions, NEPC LuCaP145.1 and ARPC LuCaP167. No correlation was found between $^{18}$FDG uptake and *FOLH1,* matching the discordance between $^{18}$FDG-PET and PSMA imaging observed in the clinic (*19*).

$^{18}$FDG uptake is restricted to assessing glucose uptake and phosphorylation and lacks sensitivity for other, more downstream metabolic processes. In contrast, hyperpolarized MRI specifically measures the forward flux of pyruvate conversion to lactate through lactate dehydrogenase, providing a more direct means to evaluate a glycolytic phenotype compared to $^{18}$FDG uptake (Fig 1C). Similar to $^{18}$FDG uptake, there was a high variability between samples with a clear division between high and low pyruvate-to-lactate conversion that did not correlate well with adenocarcinoma/NEPC phenotypes. No correlation was found between $^{18}$FDG uptake and lactate/pyruvate flux, demonstrating that glucose uptake in these models is not correlated with aerobic glycolysis (Warburg physiology) (Fig. 1D).

### Castration resistant PDX models show higher uptake of $^{18}$FDG and lower pyruvate to lactate conversion compared to their castration sensitive counterparts

The complex genomic variability among clinical ARPC and PDX ARPC models leads to too many variables in making direct comparisons between independent castration-resistant and -sensitive models. The extent of metabolic reprogramming during disease progression can be found more directly by investigating the longitudinal changes in experimentally castrated PDX-derived models. In line with reported clinical findings (*15*), the castration-resistant (CR) models LuCaPs136CR and 167CR exhibited higher retention of $^{18}$FDG compared to their castration-sensitive (CS) counterparts, LuCaPs 136 and 167 (Figs. 1D, S1B and C). In contrast, the castration sensitive models displayed relatively high pyruvate to lactate conversion compared to their castration resistant counterparts.

### AR expression is maintained after *RB1/TP53* knockdown *in vitro*

The models in Fig. 1 incorporate a wide range of prostate cancer phenotypes in a variety of genetic contexts. To more narrowly look at the specific effect of *RB1* and *TP53* on molecular imaging in an androgen sensitive cell line, we used CRISPR/CAS9 knockout of *RB1* and/or *TP53* in LNCaP cells. In this model, both *RB1* and *TP53* expression were effectively null (Fig. S2B), confirming it as an efficient model of *RB1* and *TP53* knockdown. To examine the effects of *RB1* and/or *TP3* loss in a CRPC cell

line, we introduced stable short hairpin RNAs (ShRNAs) targeting *RB1* and *TP53* into LuCaP 167 PDX-derived organoids (*18*). The LuCaP 167 PDX model was established from a liver metastasis taken from a patient with abiraterone-, carboplatin- and docetaxel-resistant CRPC (*20*). Doxycycline-induced shRNA effectively depleted *RB1* transcription in LuCaP 167, while shRNA induction reduced but did not eliminate the expression of TP53 (Fig. S2A). LuCaP 167 constitutively expresses high levels of the androgen receptor splice variant AR-V7, implying AR dependent disease progression (*21*). Expression of AR was retained upon depletion or loss of *RB1* and/or *TP53* compared to the control, while expression of the AR downstream target KLK3 decreased after doxycycline induction of *RB1* (Fig. S2C). This is consistent with previous reports that while inactivation of *RB1* suppresses AR signaling, AR expression is maintained after *RB1* loss in CRPC (*14*).

### *RB1/TP53* knockdown does not affect $^{18}$FDG uptake in LNCaP models *in vitro* or LuCaP PDX mouse models

In the castration sensitive, AR dependent LnCaP cell line, CRISPR/CAS9 knockout of *RB1* or *TP53* did not affect $^{18}$FDG uptake *in vitro* (Fig. S3). To include the effect of the tumor microenvironment, we evaluated $^{18}$FDG PET scans in *RB1/TP53* altered LuCaP 167 organoid-derived PDX CRPC tumors. $^{18}$FDG PET scans demonstrated substantial FDG uptake that appeared to be insignificantly different in *RB1/TP53* depleted compared to controls (Figs. 2 and S4C and D). To get a more precise measurement of FDG uptake, we excised these tumors after the scan and measured tissue uptake with a gamma counter. There was no significant difference between *RB1*, *TP53,* and *RB1/TP53* altered groups (Fig S4E-G) in FDG activity. Thus, *RB1/TP53* knockdown did not result in a significant change in $^{18}$FDG uptake in either model tested.

### Basal respiration and glycolytic activity are increased following decreased RB1 expression

Because *RB1* loss often is associated with increased glycolysis, we used Seahorse assays to characterize the metabolic phenotype of *RB1* and/or *TP53* altered organoids. Basal and maximal respiration were significantly elevated for both *RB1* and *RB1/TP53* alterations compared to the control for both LuCaP167 organoids and LnCaP cells (Fig. 3A and C). The basal and maximal respiration of the combined *RB1/TP53* alterations was significantly higher than *RB1* only, while partial depletion of *TP53* in LuCaP167 or complete loss of *TP53* in LNCaP resulted in no change. Extracellular acidification (ECAR), a measure of proton efflux from both glycolysis and respiration and a surrogate for lactate export, was also higher in *RB1* and *RB1/TP53* altered models (Fig. 3B and D).

The large increase in the extracellular acidification rate in the combined *RB1/TP53* modified models is characteristic of an increased glycolytic phenotype, as meeting a steady-state ATP demand exclusively by glycolysis is considerably more acidifying than meeting the same demand strictly by oxidative phosphorylation. To further analyze the mechanism of increased acidification, we evaluated the enzymatic activity of lactate dehydrogenase (LDH) (Fig. 4), the enzyme that converts pyruvate to lactate. Consistent with the Seahorse assays, increased LDH activity was observed upon depletion or loss

of *RB1* in both models. Overall, the data is consistent with the loss of *RB1* with and without *TP53* loss leading to increased metabolic activity.

**Combined *RB1/TP53* depletion leads to metabolic changes, including a diversion of glucose into glycogenesis**

To gain a more comprehensive understanding of the metabolic transformation after *RB1* and/or *TP53* depletion, we quantified the downstream metabolites of $^{13}$C glucose in the LuCaP 167 CRPC organoid model by NMR (Fig S5). $^{13}$C glycogen was highly enriched after dual *RB1/TP53* depletion while steady state concentrations of $^{13}$C glucose decreased, suggesting a diversion of glucose to form glycogen. It also is of interest that glutamine levels increased since glutamine utilization has been shown to suppress glucose uptake in various cancer models (*22*). $^{13}$C UDP-glucose, an important intermediate of the pentose phosphate pathway leading to glycogenesis, was found in high abundance but was unaffected by either *RB1* or *TP53* depletion. Consistent with the Seahorse and LDH activity assays, $^{13}$C labeled lactate concentrations were elevated after dual *RB1/TP53* depletion with more modest increases occurring following single gene modifications. In the non-polar fraction, both cholesterol synthesis and $^{13}$C incorporation into lipid acyl chains and glycerol headgroups were significantly elevated after depletion of either *RB1* or *TP53*.

When measured by $^{13}$C NMR, glucose metabolism in the androgen sensitive LnCaP model was less affected by *RB1/TP53* loss relative to castration resistant LuCaP167 (Fig S6). Out of the 12 metabolites whose $^{13}$C incorporation was high enough to be quantified by $^{13}$C HSQC 1D NMR, only glycogen and cholesterol showed significant (roughly 3-fold) differences after loss of both *RB1* and *TP53*. This is not evidence that other changes did not occur as $^{13}$C NMR has limited sensitivity and is only able to detect metabolites with high steady-state concentrations. We therefore repeated the $^{13}$C glucose tracer experiment using targeted IC-MS to detect changes in intermediates in the glycolytic and TCA pathways whose low abundance is problematic for NMR.

In the LuCaP 167 organoid models, *RB1* and *TP53* depletions were clearly differentiated from control samples by IC-MS (Figs. 5A, S5, and S7), primarily by a decrease in pyruvate and an increase in lactate concentrations. Intermediates in the latter half of the TCA cycle decrease upon depletion of either *RB1* or *TP53*. Glucose-1-Phosphate, one of the intermediates of glycogenesis, was robustly increased following *RB1* depletion. Thus, both $^{13}$C HSQC 1D NMR and IC-MS detected many of the same metabolite concentration shifts seen with $^{13}$C NMR.

The primary difference in metabolic reprogramming for the LnCaP cells was observed in the combined *RB1/TP53* null samples (Figs. 5B and S8). Dual *RB1/TP53* knockout increased activity throughout the TCA cycle, which was not seen to a significant extent with individual knockouts. Consistent with the $^{18}$FDG uptake data, levels of glucose-6-phosphate were unchanged following *RB1* and/or *TP53* alterations. The glycogenic intermediate, glucose-1-phosphate was increased, as expected from the $^{13}$C HSQC 1D NMR results.

To summarize, *RB1* loss in different ARPC models led to consistent changes specifically, 1) increased lactate, reflecting higher lactate dehydrogenase activity, 2) increased glucose-1-phosphate and glycogen levels, suggesting redirection of glucose

metabolism to gluconeogenesis, and 3) modulation of the TCA cycle, specifically a consistent increase in αKG across models in addition to other model-specific changes.

### Increase in LDH flux after *RB1* knockdown can be detected in vivo by $^{13}$C-HPMRS

NMR and ICMS identified several metabolites that were upregulated after *RB1/TP53* alteration. To determine whether pyruvate to lactate flux imaging could be a tractable approach to analyzing such a phenotype *in vivo*, we first assayed hyperpolarized $^{13}$C-pyruvate conversion in genetically modified LnCaP cells in vitro (Fig. S9A). We observed increased pyruvate flux to lactate in *RB1* null cells and an additional increase in combined *RB1/TP53* null cells, but no change in *TP53* null only cells. To extend this data, we assayed LuCaP167 organoid-derived PDX tumors *in vivo* (Fig. 6) using magnetic resonance spectroscopy to detect the de novo generation of new metabolites from pyruvate. In LuCaP 167 tumors, the rate of pyruvate to lactate conversion reflective of LDH flux was significantly increased with depletion of *RB1*(see Fig. S9B) with or without partial depletion of *TP53*. We conclude that measuring lactate flux may be marker of *RB1* modified tumors, which are known to be associated with rapid progression.

## Discussion

CRPC is a highly heterogeneous tumor type with variability not only in the underlying genomic landscape but also in the lineage phenotype (*9,10*). Although tumor imaging modalities can be powerful methods to both detect tumors and gain additional predictive or prognostic information, it is important that such findings be validated at a molecular level. Here we take advantage of a large cohort of tractable, reproducible organoid models to evaluate for the first time the distribution of glycolytic phenotypes among multiple phenotypically and genetically characterized models (*18,23*) using assays that quantify initial and final steps in glycolysis, FDG uptake and pyruvate to lactate conversion, respectively. Although the highest levels of FDG uptake were observed in ARPC while uptake in NEPC models was generally minimal, we found that FDG cannot distinguish between ARPC or NEPC lineage phenotypes *in vitro* due to substantially overlapping ranges in values.. This is consistent with the previously described role of AR in stimulating the expression of glycolytic proteins (*4,5*). Of particular interest, there was a clear lack of correlation between glucose import and lactate production, indicating that FDG uptake is not necessarily related to aerobic glycolysis (Warburg physiology) (Fig. 1D). Experimental models have shown that lactate production and glucose import are modulated in parallel directions in response to genetic manipulation (*24*). However, it is perhaps not unexpected that intermediary metabolites connected as they are by multiple pathways have differences in rate limiting steps among patient-derived samples.

PSMA-PET has become a widely used marker of prostate cancer and generally identifies ARPC and CRPC. It has been observed that PSMA uptake can be reduced or completely suppressed in the later stages. It is usually the case that in advanced PSMA-negative prostate cancer, FDG PET in the same lesions is positive, and these discordant cases portend a worse prognosis (*26,27*). Since PSMA PET is most valuable in PSMA-directed therapies, i.e., PSMA-targeted radioligand therapy, PSMA-/FDG+ discordant cases predict poorer outcomes, although the importance of this discordance

has been recently questioned (*28*). Independent of PSMA PET, FDG PET uptake is associated with a poorer prognosis in prostate cancer (*29*). Functional *RB1* loss in CRPC is the most significant predictive mutation with respect to both poor survival and lack of AR signaling inhibitor drug responsiveness for adenocarcinoma pathologies (5). In addition, *RB1* and *TP53* loss of function is highly associated with lethal AR negative NEPCs. To address whether loss of *RB1* and/or *TP53* in the context of adenocarcinoma leads to increased FDG uptake and/or glycolysis, we analyzed two AR+ adenocarcinoma models that were genetically depleted for these molecules.

We determined that *RB1/TP53* loss was associated with increased extracellular acidification, a measure of glycolytic lactate production, and increased oxygen consumption, a measure of oxidative phosphorylation (Figure 3). Consistent with this, LDHA enzyme activity (Figure 4) was increased, as was cellular lactate itself (Figure 5), as determined by ICMS. Increased expression of LDHA and MCT4, the lactate efflux transporter, have been described for prostate cancer progression in experimental models and clinical samples (*3,30*). Other properties that were observed in both models included increased glucose diversion into glycogen synthesis and increased membrane lipid synthesis. We assessed whether quantitative changes to FDG or HP-MRI imaging were correlated with the genomically-driven metabolic alterations in glycolytic phenotype. Consistent with increased lactate production, $^{13}C$ HP-MRI spectroscopy signals were increased following *RB1/TP53* depletion. On the contrary, FDG uptake values remained the same. These data suggest that LDHA-dependent lactate production was rate-limiting relative to *RB1* expression, although glucose availability was not.

Clinical experience has been that increased FDG uptake in CRPC is associated with poor survival. We show poor correlation between FOLH1 expression and FDG uptake indicating that PSMA scans cannot be used to predict FDG uptake. Further, we show here that cancer cells themselves do not demonstrate increased FDG uptake as in *RB1/TP53* null NEPC organoids derived from patients or as ARPC organoids in which *RB1/TP53* were depleted. How does one explain the observation that clinical FDG uptake is increased in neuroendocrine and other advanced prostate cancer phenotypes, while our investigation shows that FDG uptake was unchanged despite genetic alterations associated with poor survival of ARPC and a high rate of transition to NEPC? The answer may well lie in the fact that cancer cells are not the only cell type found within tumors. FDG uptake has been shown to be highly dependent on microenvironmental host immune cells such as myeloid-derived macrophages and activated T cells (*22*). These cells are glucose avid and tend to outcompete the tumor cells for glucose uptake in the context of the tumor microenvironment. Importantly, acidic tumor microenvironments secondary to lactate accumulation promote M2 macrophage and Treg differentiation while suppressing T effector cell function, leading to an immunosuppressive microenvironment (*31*). These activated TME cells are metabolically active and likely take up FDG avidly. It will be of interest in the future to determine in clinical samples whether there are correlates between 1) advanced prostate tumors with decreased AR signaling and/or 2) *RB1* loss of function, acidic tumor microenvironments, increased M2 macrophage numbers, and associated increased FDG uptake.

## Materials and Methods:

### 3D Organoid culture

LuCaP PDX tumors were maintained at the NCI under the NCI Animal Care and Use Committee approved protocol (LGCP-003-2-C) and validated using STR analysis by Laragen, Inc. For processing, tissue was cut into small pieces, 2 to 4 mm, with a scalpel blade. The tissue was then collected in advanced DMEM/F12 with 10 mmol/L HEPES and 2 mmol/L Glutamax, transferred to gentle MACS C tubes (Miltenyi Biotec: #130-096-334) and digested using the Tumor Dissociation Kit for human tissue (Miltenyi Biotec: #130-095- 929) on a gentle MACS Octo Dissociator with heaters (Miltenyi Biotec: #130-096-427), program 37C_h_TDK_2. Processed samples were centrifuged, resuspended, and passed through a 100-µm cell strainer as needed to eliminate macroscopic tissue pieces. For PDXs, cell pellets were resuspended in two to three volumes of ACK lysis buffer (Lonza: #10-548E) according to the manufacturers' specifications, and washed cells were resuspended in media.

PDX tumors maintained at the NCI were passaged in NODscid gamma (NSG) mice. After processing as described above, cell suspensions ($2*10^6$ cells) were mixed with growth factor-reduced, phenol red-free Matrigel (BD Biosciences: #356231) and injected subcutaneously.

To culture PDX-derived cells as organoids, cell suspensions, processed as described above, were plated in 3D on a 10 cm dish, 6 and 96 well plates in 5% matrigel. Growth media formulation for PrENR is described in Drost and colleagues (*32*). For passaging, organoids were incubated with dispase, dissolved in advanced DMEM/F12 to a final concentration of 1 mg/mL, and incubated for 2 hours at 37℃. Pelleted organoids were resuspended in prewarmed TrypLE Express (Thermo Fisher: #12605028) for approximately 5 minutes at 37℃ with periodic pipetting. The resulting cell suspensions were diluted in advanced DMEM/F12, centrifuged, resuspended, and plated as described previously.

### 2D Cell Culture

LNCaP cells were purchased from ATCC and were cultured in RPMI with 10% FBS as described previously (*33*).

### Lentiviral transduction

A total of $2*10^6$ cells were transduced with various lenti e.g., SMARTvector Inducible Human Non-targeting Control, *RB1* and *TP53* shRNA (Dharmacon Reagents) and pLX313-Renilla Luciferase (addgene; #118016) by spin infection at 1200 rpm for 90 minutes at room temperature. Cells were incubated overnight in the presence of the virus. Cells were then collected and replated in 3D in Matrigel as described previously (*18*). Further cells were selected against the prescribed antibiotic with 2.5 µg/mL of puromycin and hygromycin respectively, for stable cell line.

### *RB1* and/or *TP53* LNCaP CRISPR-Cas9 knock-out.

For CRISPR mediated *RB1* and *TP53* gene deletion, we used *RB* and *TP53* guide sequence AAGTGAACGACATCTCATCTAGG and TATCTGAGCAGCGCTCATGGTGG (g)RNA respectively designed by the Broad Institute sgRNA designer. Blasticidin-

resistant Cas9 along with sgRNA and GFP plasmids were electroporated in LNCaP and the cells were cultured for 72 hr. After 72 hrs, single GFP positive cells were sorted and grown as a monoclones for *RB1, TP53* and *RB1/TP53* Crispr KOs. Since WB showed that the expression of *RB1* and *TP53* proteins was completely abolished for all clones, we used only clone C1 of RB1 and/or TP53 Crispr KOs in subsequent experiments.

**Generation of *RB1*, *TP53* altered PDX system**

*RB1*, *TP53* and *RB1/TP53* altered LuCap 167 PDX tumors were generated in 6-week-old NODscid gamma (NSG) mice by subcutaneously injecting *RB1*, *TP53*, *RB1/TP53* altered organoids ($2*10^6$ cells) mixed with growth factor–reduced, phenol red–free Matrigel (BD Biosciences: #356231) under an NCI Animal Care and Use Committee approved protocol (LGCP-003-2-C). As the tumor started to grow mice were randomized and put in two different groups [*RB1*, *TP53*, or *RB1/TP53* (control) and (depleted)]. Mice were given an IP injection of 100ml of saline (control) or 100 ml of 0.2 mg/ml of doxycycline prepared in saline**,** twice weekly until the tumor reaches 1-1.2 cm in diameter. Tumor volume was measured with a digital caliper once weekly. LuCaP PDX tumors were validated using STR analysis by Laragen, Inc.

**Whole Cell Lysate Preparation for Protein Expression**

Organoids were grown for 0, 2, and 3 weeks with or without (1 µg/ml) of doxycycline (EMD Millipore: #324385), organoids were harvested and washed twice with cold PBS. Alternatively, LNCaP Crispr knockout were harvested with TrypLE and washed twice with cold PBS. Cell pellets were processed in 1% SDS or RIPA/NP40 lysis buffer containing protease and phosphatase inhibitors. After 45 mn of suspension at 4℃, pellets were sonicated (Sonication 40-45% amplification, 5 cycles, 1 sec on/off at 4℃). WCL lysate was centrifuged at 10000 rpm for 10mn, and protein estimates were done using BCA analysis (Pierce Kit: #23225) according to manufacturer's instructions.

**Immunoblotting**

15-30 µg of protein lysate was separated on 4% to 20% mini-gradient gels and transferred onto polyvinylidene difluoride membranes (PVDF). Membranes were blocked in 5% milk (Cell Signaling: #9999) in TBST, followed by overnight antibody probing at $4^oC$ with RB1 (CST: #9309S), TP53 (Abcam: #PAb240), AR (CST: #5153S), LDH (Novus: #NBP1-48336), KLK3 (CST: #5365), and Histone-H3 (CST: #4499S). After primary washing, blots were reprobed with HRP labelled secondary antibodies for an hour at 25℃. The blots were washed with TBST thrice for 5min and developed with Bio-Rad (Chemiluminescence system).

**LDH activity assay**

LDH activity was measured using the LDH assay kit (Bio Vision: # K726-500) according to the manufacturer's instructions. Cell lysates were prepared in the buffer provided with the kit, equal protein samples were diluted in 50µl of the buffer and incubated at room temperature for 10 min. The lysates were further mixed with a reaction mixture (50µl reaction mix), containing 48µl of development buffer and 2µl of development enzyme mix and dispensed onto 96-well microplate. OD was measured at 450 nm from both samples and standard with the help of an ELISA plate reader (TECAN pro200,

Männedorf, Zürich, Switzerland) at room temperature. Results were plotted as fold change over control.

**Organoids quantification assays**

Organoids ($2.5*10^3$ cells/well respectively) were seeded in wells (technical replicates) in 3D on 96-well plates and cultured for the indicated number of days in presence or absence of doxycycline supplemented media. Quantification was performed using Renilla glow (Promega: #G9681) according to the manufacturer's protocol.

**Seahorse Assay**

Extracellular acidification rate (ECAR) and Cellular oxygen consumption rate (OCR) was measured with a Seahorse XF96e bioanalyzer (Seahorse Bioscience) using a Glycolytic Rate Assay Kit (Agilent Technologies: #17394939A) according to manufacturer's instructions. Organoids and LNCaP Crispr KOs ($2.5*10^2$ and $10^4$ cells/well respectively) were seeded in wells (technical replicates) each of a Seahorse XF 96-well assay plate in full growth medium. Post 3rd day, organoids were supplemented with growth media containing doxycycline (1 µg/ml). Media were replaced twice weekly until 21 days. Alternatively, after 48hr of seeding LNCaP monoclonal Crispr KOs, the medium was carefully washed and replaced with prewarmed sea horse running medium (consisting of nonbuffered DMEM, Agilent Technologies) supplemented with 1 mmol/L sodium pyruvate, 2 mmol/L glutamine, and 10 mmol/L glucose, pH 7.4). Plates were incubated for 60 minutes in a non-$CO_2$ incubator at 37°C before 12 basal measurements were undertaken. Rot/AA (0.5 mmol/L, inhibitors of mitochondrial electron transport chain) was immediately added followed by three further measurements, 2-deoxy-D-glucose (2-DG), a glucose analog which inhibits glycolysis through competitive binding of glucose hexokinase, was then added with another three further measurements. Post assays organoid or cell numbers were calculated from each well with Renilla glow or Cyquant assays for RB1-TP53 altered organoid culture or LNCaP monoclonal Crispr KOs. Results from each well were normalized with respective cell number from the well.

**Sample Preparation for Stable isotope resolved metabolomics (SIRM)**

Organoids and LNCaP monoclonal Crispr KOs were seeded in 10 cm dishes at 2 million cells per dish, incubated in complete medium. Post 3 days complete media from organoid culture was supplemented with doxycycline (1µg/ml) for 21 days. Media was replaced twice weekly until 21 days. Post 21-day, organoid cultures were washed with PBS and media was replaced with DMEM (Dulbecco's Modified Eagle's Medium) medium containing 15 mM [U-13C]-glucose (Cambridge Isotope laboratories: #CLM-1396-10), 2 mM unlabeled glutamine, and 10% dialyzed FBS (in triplicate), or unlabeled media (15 mM natural abundance glucose; single plate), at 37°C in a 5% CO2 atmosphere, RH > 90% for 48hr (approximately one cell doubling). Alternatively post 48 hr LNCaP monoclonal CRISPR KOs were washed with PBS and media was replaced with DMEM (Dulbecco's Modified Eagle's Medium) medium containing 10 mM [U-13C]-glucose (Cambridge Isotope laboratories: #CLM-1396-10), 2 mM unlabeled glutamine and 10% dialyzed FBS (in triplicate), or unlabeled media (single plate), at 37°C in a 5% $CO_2$ atmosphere, RH > 90% for 24hr (approximately one cell doubling). Glucose

concentrations in fresh media were verified by immobilized enzyme electrode amperometry using a YSI 2950 Bioanalyzer. After incubation, the medium was aspirated, and the cells (6-8 million per plate) were washed twice with ice cold PBS and then quenched on the plate with acetonitrile as previously described. Metabolites were extracted using the Fan Extraction Method (*34*) with aqueous fractions for NMR and mass spectrometry lyophilized and stored at -80°C until analysis, while the organic fraction was stored at -80°C in chloroform in the presence of butylated hydroxytoluene (BHT). A polar fraction in a 200 µL $D_2O$ solution containing 0.25 µM DSS-d6 as reference and concentration standard. For each sample, a 1D $^1$H Presat and $^1$H-$^{13}$C HSQC spectra were recorded using a phase sensitive, sensitivity enhanced pulse sequence using echo / anti echo detection (*35*) and shaped adiabatic pulses (hsqcetgpsisp2.2) for the $^1$H-$^{13}$C HSQC experiments. The experiments were performed at 293K with a 16.45 T Bruker Avance Neo spectrometer using a 3 mm inverse triple resonance cryoprobe with an acquisition time of 2 s and a recycle delay of 6 s for the $^1$H experiment, and an acquisition time of 213 ms and recycle delay of 1.75 s for the HSQC experiments. Presaturation was used in each case to suppress the residual water signal. The most concentrated sample from each group was also analyzed by high-resolution 2D multiplicity-edited HSQC-TOCSY and $^1$H/$^1$H TOCSY (50 ms mixing time) with an acquisition time in $t_2$ of 1 s and a relaxation delay of 1 s and an isotropic mixing time of 50 ms (TOCSY) and an acquisition time of 0.2 s in $t_2$, recycle time of 2 s (*36*). The nonpolar spectra were acquired similarly except that one half of the nonpolar fraction was evaporated to dryness at RT and re-dissolved in 200 µL of d4-methanol (*37*). The nonpolar spectra were acquired similarly except that one half of the nonpolar fraction was evaporated to dryness at RT and re-dissolved in 200 µL of d4-methanol, and analyzed as previously described. (*38,39*)

**Mass Spectrometry analysis**

ICMS samples were prepared by dissolving the lyophilized powder of polar fractions in 50 µL of 18 MΩ water. The metabolites were separated with a Dionex ICS6000 system using modifications to the method of Sun *et al* (*37*). here the eluent was 18 MΩ water at 0.38mL/min, and the KOH gradient was generated electrolytically, then removed by the suppressor post-column. The separated metabolites were then analyzed by Orbitrap Fusion Lumos mass spectrometer (Thermo Scientific). 0.1mL/min acetonitrile was used as the make-up solvent to assist sample desolvation in the H-ESI (Heated Electrospray Ionization) source. The MS settings were: scan range(m/z) 70-800, resolution 500,000 at m/z 200, RF Lens (%) 30, sheath gas flow rate 50, auxiliary gas flow at 10, sweep gas flow at 1, ion transfer tube temperature at 325 °C, vaporizer temperature 350 °C, negative ion voltage at 2500V.

Our in-house metabolite database was incorporated into TraceFinder software (Thermo Fisher) for peak assignments and peak area measurement. 112 metabolite standards were prepared in-house and run at different concentration levels to establish calibration curves for each metabolite. Following correction for $^{13}$C natural abundance (PREMISE

software kindly provided by Dr. Richard Higashi, University of Kentucky) and split ratio of the aliquot used for analysis, the calculated amount of each metabolite was then further normalized to the protein quantity measured by BCA assay.

### $^{18}$F-FDG-PET scan

Tumor-bearing mice described under protocol (MIP-006-3-A) were injected with 100 mCi of $^{18}$F-FDG$^{+}$ in PBS via a tail vein under anesthesia. Sixty minutes after $^{18}$F-FDG$^{+}$ administration, a whole-body emission PET scan was conducted using a BioPET (Bioscan Inc.) under anesthesia with 1.5% isoflurane with a nominal resolution of 0.375 mm × 0.375 mm × 0.375 mm. Animals were euthanized upon completion of scan and tumor along with other vital organs were excised from body, weighed and biodistribution value were recorded. Total tumor volume and total $^{18}$FDG$^{+}$ activity was calculated based on the voxel size from the scan. Data was plotted as total $^{18}$FDG$^{+}$ activity from each scan as described earlier (*40*).

### Hyperpolarized $^{13}$C NMRS

Hyperpolarized 13C NMRS experiments were performed on a Spinsolve Benchtop NMR (Magritek). 15-20 million cells from freshly processed PDX tumors were seeded as a suspension culture in 75cm ultra-low attachment flask (5 million cells /Flask) in 2% matrigel to form organoids. Alternatively, 10 million cells of LNCaP monoclonal Crispr Knockouts were plated in 15cm dishes. Cells were incubated in complete medium until the number reached 40-50 million in total. Organoids or cells were collected and washed with PBS. Respective cell numbers were counted and resuspended in 450ul of media. Cell suspension was collected in an NMR tube and prewarmed at 37°C. 75 µL of 96 mmol/L hyperpolarized [1-$^{13}$C] pyruvate solution from a Hypersense DNP Polarizer (Oxford Instruments) was injected in the NMR tube. $^{13}$C two dimensional spectroscopic images were acquired on a benchtop NMR. Data was plotted as AUC of hyperpolarized-$^{13}$C-lactate/pyruvate conversion.

### Hyperpolarized $^{13}$C MRS/ MRI

Hyperpolarized 13C MRI experiments were performed on a 3T MRI Scanner (MR Solutions Inc.) using a 17-mm diameter home-built $^{1}$H/$^{13}$C coil. A 96 mmol/L hyperpolarized [1-$^{13}$C] pyruvate solution from a Hypersense DNP Polarizer (Oxford Instruments) was administrated under anesthesia with 1.5% isoflurane via a tail vein cannula (12 mL/g body weight) described under animal protocol (RBB-159-3-P). $^{13}$C two-dimensional spectroscopic images were acquired with a 32 × 32 mm field of view in an 8-mm axial slice (*41*).

### Statistical analysis

All experiments were performed with at least three biological replicates per condition. Data are displayed as mean ± SEM. Statistical significance (a < 0.05) was determined using Student *t* test, one-way ANOVA on GraphPad Prism Software as appropriate.

### Acknowledgements

This project has been funded in whole or in part with federal funds from the National Cancer Institute, National Institutes of Health, under Contract No. 75N91019D00024.

The content of this publication does not necessarily reflect the views or policies of the Department of Health and Human Services, nor does mention of trade names, commercial products, or organizations imply endorsement by the U.S. Government.

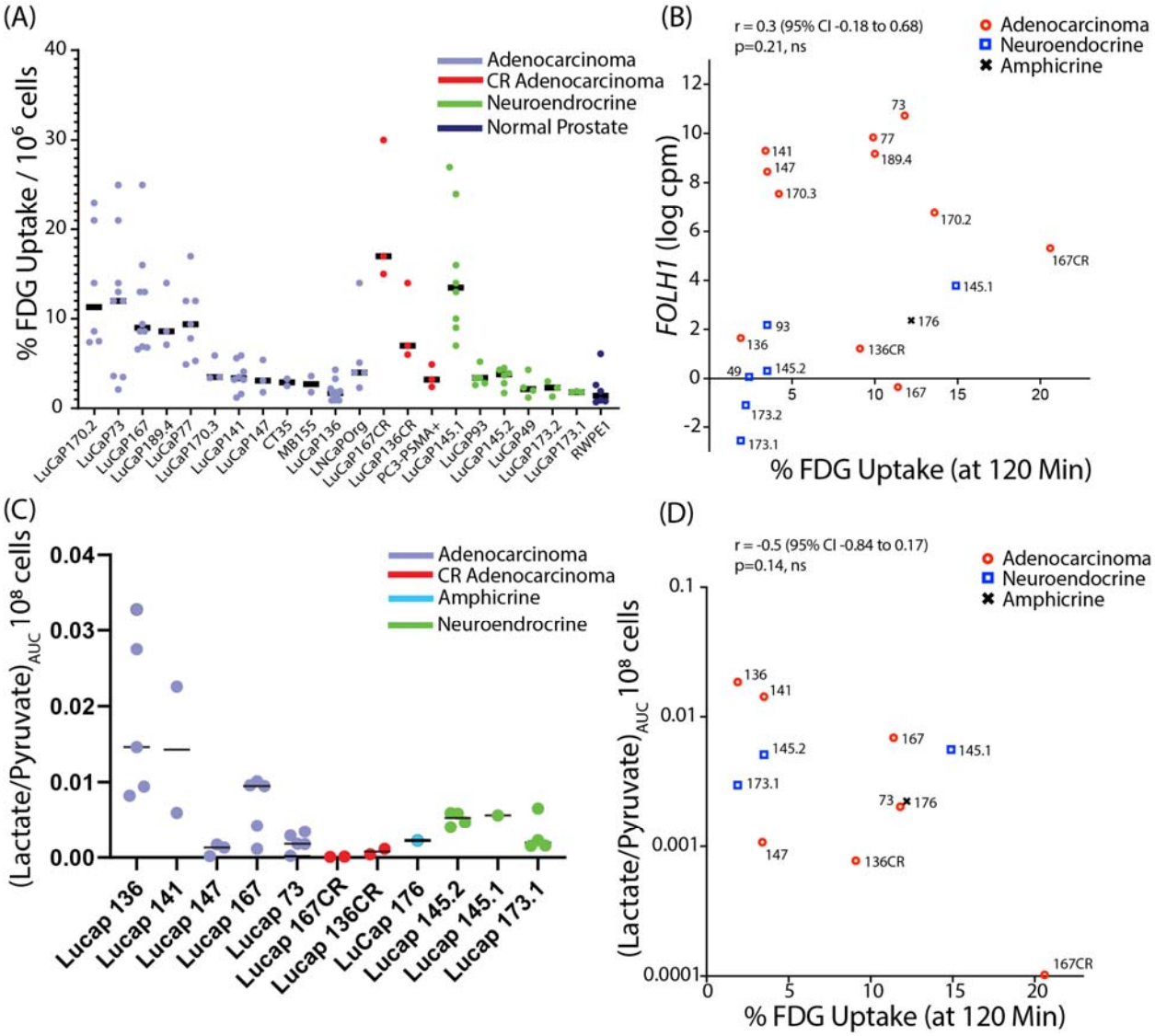


**Figure 1. $^{18}$FDG uptake does not correlate with hyperpolarized $^{13}$C lactate/pyruvate conversion** **A.** Percent $^{18}$FDG uptake at the final timepoint of 120 minutes for biological replicates of the same model. **B.** Pearson correlation of $^{18}$FDG uptake at the final timepoint (120 minutes) against *FOLH1* transcription (cpm) in LuCaP organoids **C.** AUC of hyperpolarized-$^{13}$C-lactate/pyruvate conversion in LuCaP

organoids. **D.** Scatterplot of $^{18}$FDG uptake at the final timepoint (120 minutes) against the AUC of hyperpolarized-$^{13}$C-lactate/pyruvate conversion in LuCaP organoids.

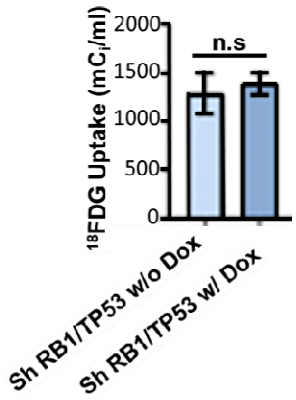


**Figure 2. Combined *RB1*/*TP53* knockdown does not affect $^{18}$FDG uptake in CRPC mice xenografts.** Total $^{18}$FDG activity in LuCaP 167 organoids PDX mouse xenograft models with (n=7) or without (n=3) induction of shRNA targeting *RB1* and *TP53* by doxycycline.

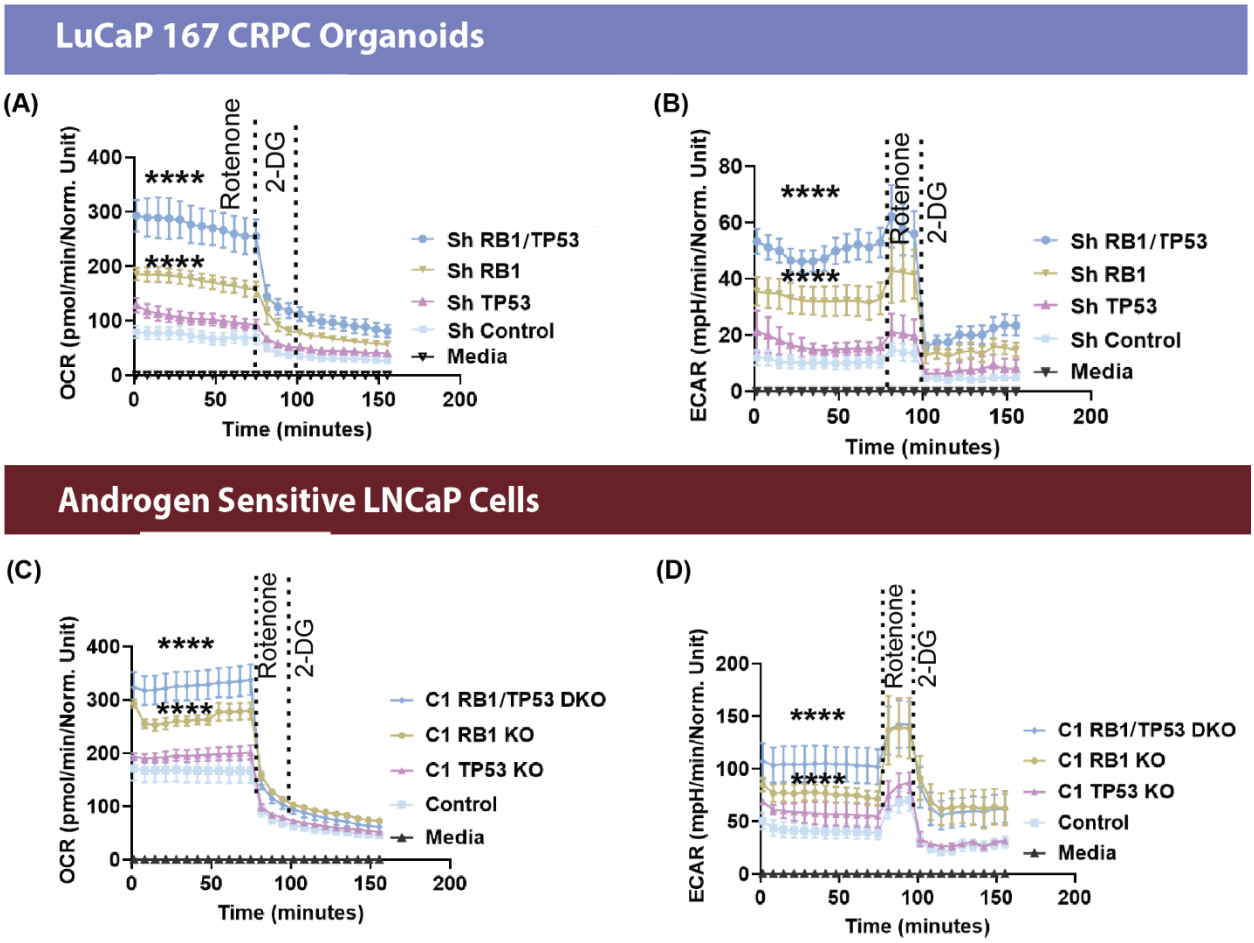


**Figure 3. Depletion of *RB1* alone or combined with *TP53* elevates basal respiration rates and increased glycolytic activity** (**A)** Oxygen consumption rate (OCR) and (**B)** extracellular acidification rate (ECAR) of LuCaP167 organoid cultures either with 3 weeks of doxycycline induction of shRNA targeting *RB1* and / or *TP53* or without (control). using a Glycolytic Rate assay kit on a Seahorse XF96e analyzer. **(C and D)** OCAR and ECAR performed with *RB1* and/ or *TP53* genetically-modified LNCaP Crispr KOs. Data are represented as mean ± SEM, n=3 expr. ns = not significant. One-way ANOVA test with Dunnett's multiple comparisons test was performed using Prism 9.0. p= * (0.05), ** (0.01), *** (0.001).

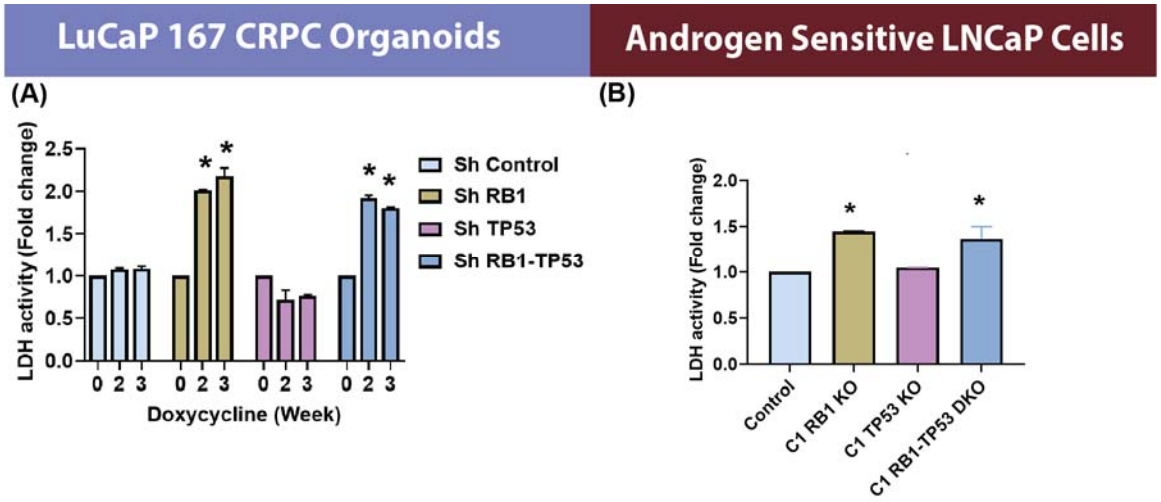


**Figure 4. RB1 depletion leads to increased LDH activity in both CRPC and androgen sensitive models.** ELISA based LDH activity of **(A)** LuCaP167 organoids with or without ShRNA targeting *RB1* and/or *TP53*, and **(B)** LNCaP Crispr-mediated knockout (KO) of *RB1* and/or *TP53*. One-way ANOVA test with Dunnett's multiple comparisons test was performed using Prism 9.0. p= * (0.05), ** (0.01), *** (0.001).

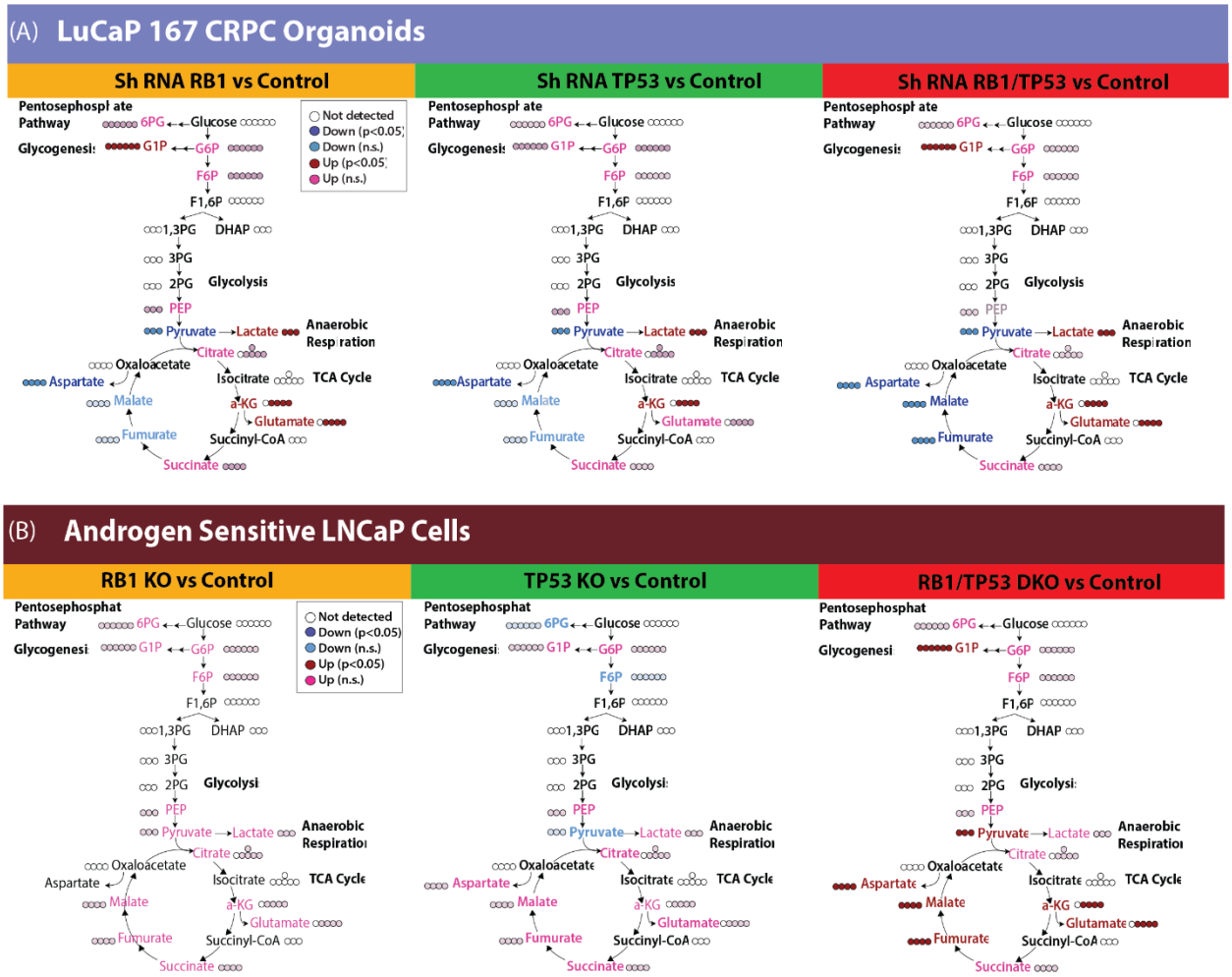


**Figure 5. Metabolic changes upon *RB1* and/ or *TP53* depletion by ICMS. A.** LuCaP167 organoids either with or without ShRNA targeting RB1 and/or TP53 **(B)** LNCaP Crispr-mediated knockout (KO) of RB1 and/or TP53

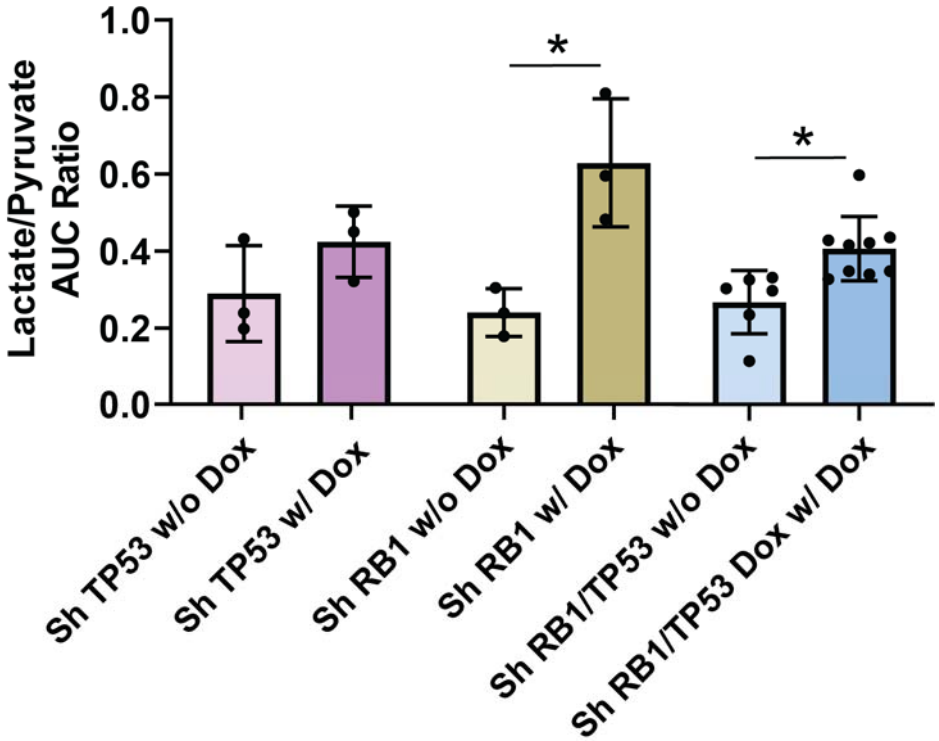


**Figure 6. $^{13}$C-HPMRS shows depletion of *RB1* alone or combined with *TP53* depletion increases LDH flux in vivo.** *In vivo* LDH activity in LuCaP 167 organoids PDX mouse xenografts with or without doxycycline inducible shRNA knockdown of *RB1* and/ or *TP53* calculated from time resolved $^{13}$C hyperpolarized non-localized spectra from the ratio of the area under the lactate and pyruvate signals. Data are represented as mean ± SEM, ns = not significant Student t test was performed using Prism 9.0. p= * (0.05), ** (0.01), *** (0.001).

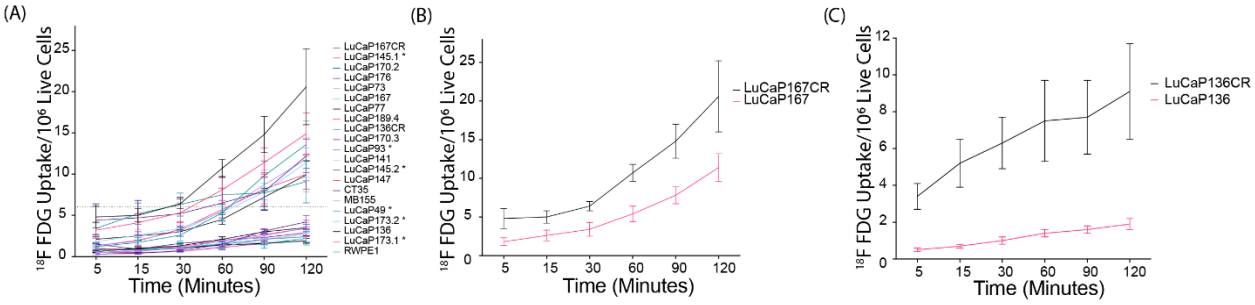


**Supplementary Figure 1. Adenocarcinoma, castration-resistant prostate cancer models display higher FDG uptake**. **(A)** FDG uptake over time per model; % uptake / $10^6$ live cells = [(cpm uptake) / (cpm total added) x (live cells total added)] x ($10^6$live cells) x 100) for each timepoint. Line denoting the 6% FDG uptake indicates the separation between FDG-high models and FDG-low models. **(B, C)** FDG uptake over time comparing castration sensitive parental and experimentally-selected castration resistant (CR) PDX-derived organoid models.

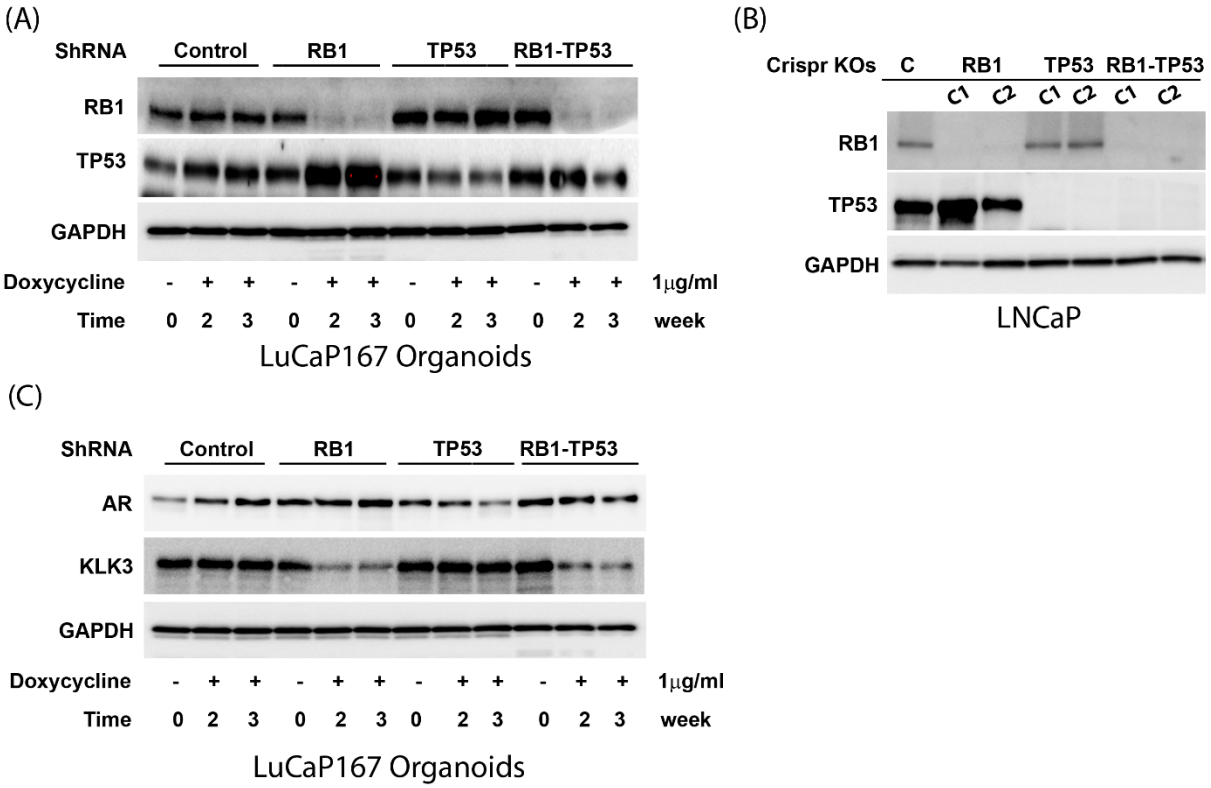


**Supplementary Figure 2. *RB1* and/ or *TP53* depletion maintains AR expression.** (**A)** Western blot showing RB1, TP53 and GAPDH protein expression in *RB1* and/or *TP53* altered LuCaP167 organoid cultures after 0, 2, or 3 weeks of ShRNA induction by doxycycline. **(B)** Western blot showing RB1, TP53 and GAPDH protein expression in *RB1* and/or *TP53* LNCaP Crispr KOs. **(C)** Western blot showing AR, KLK3 and GAPDH protein expression in *RB1* and/or *TP53* altered 167 LuCaP organoid cultures post 0, 2, or 3 weeks of doxycycline induction.

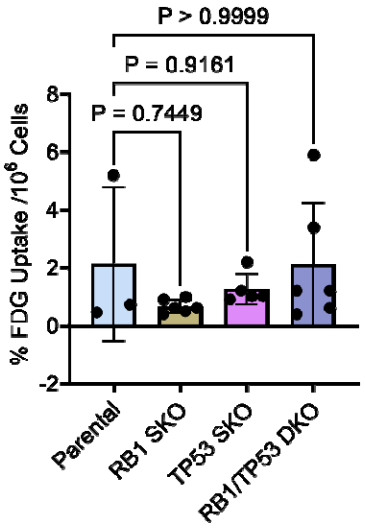


**Supplementary Figure 3. *RB1* and/ or*TP53* knockdown does not affect**: **$^{18}$FDG$^{+}$ uptake in LnCaP monoclonal Crispr knockouts.** $^{18}$FDG uptake per million cells after 120 minutes CRISPR/CAS9 knockout of *RB1* and/or *TP53*.

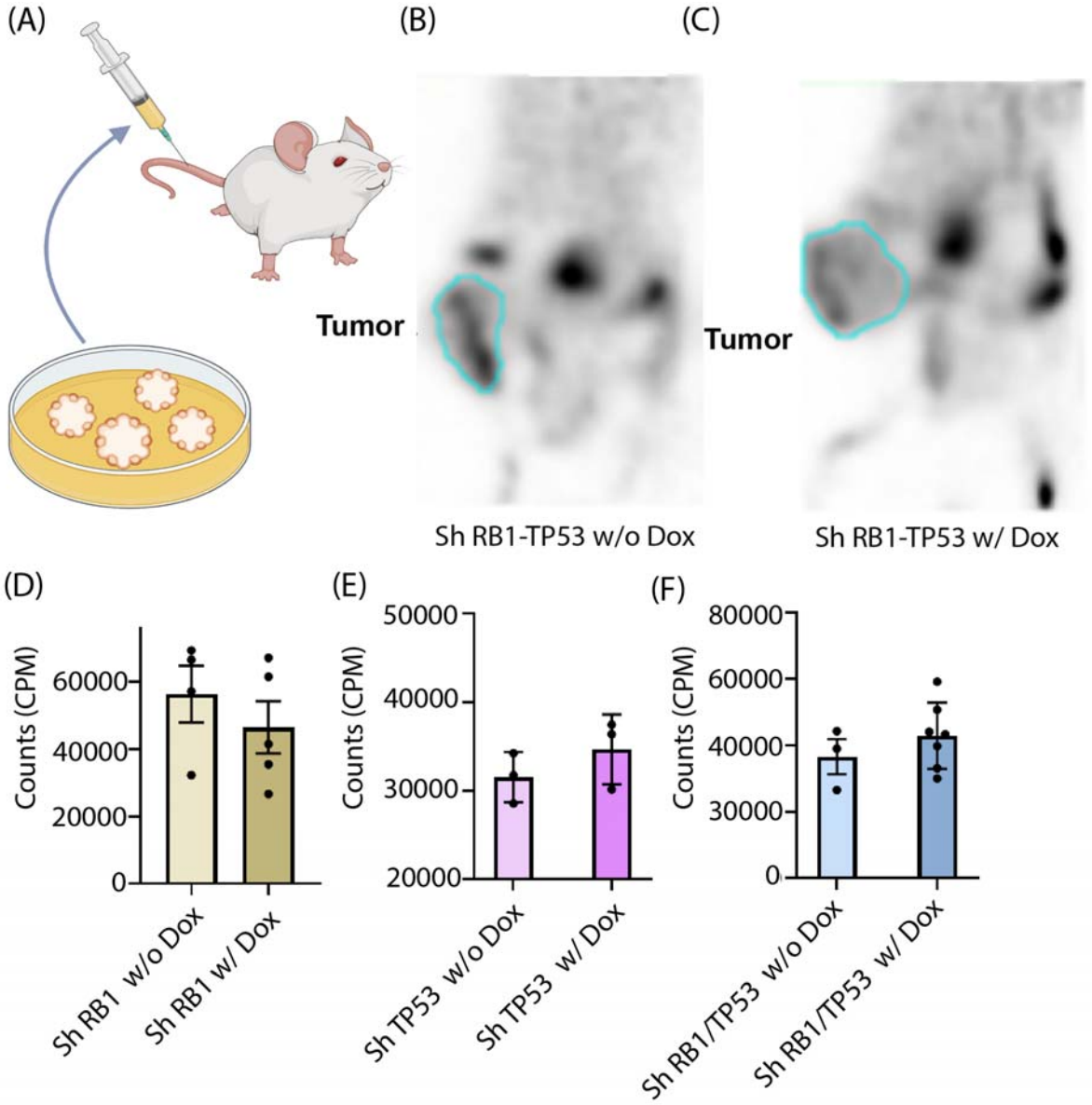


**Supplementary Figure 4. *RB1* and/ or*TP53* loss does not affect $^{18}$FDG$^{+}$ uptake in a LuCaP PDX model. (B and C)** $^{18}$FDG$^{+}$-PET scan image showing total $^{18}$FDG$^{+}$ activity present inside LuCaP (PDX) mouse CRPC xenograft models with and without induction of shRNA targeting *RB1* and *TP53* by doxycycline. **(D, E, F)** Total amount of $^{18}$FDG$^{+}$ calculated in scintillation counter from excised tumors with shRNA targeting *RB1* (n=5), *TP53* (n=3), *RB1/TP53* (n=7) induced by doxycycline, and their respective controls without doxycycline induction (n=4, 3, 3). Difference between control and knockdowns were not statistically significant. Data mean ± SEM, ns = not significant. Student t test was performed using Prism 9.0. p= * (0.05), ** (0.01), *** (0.001).

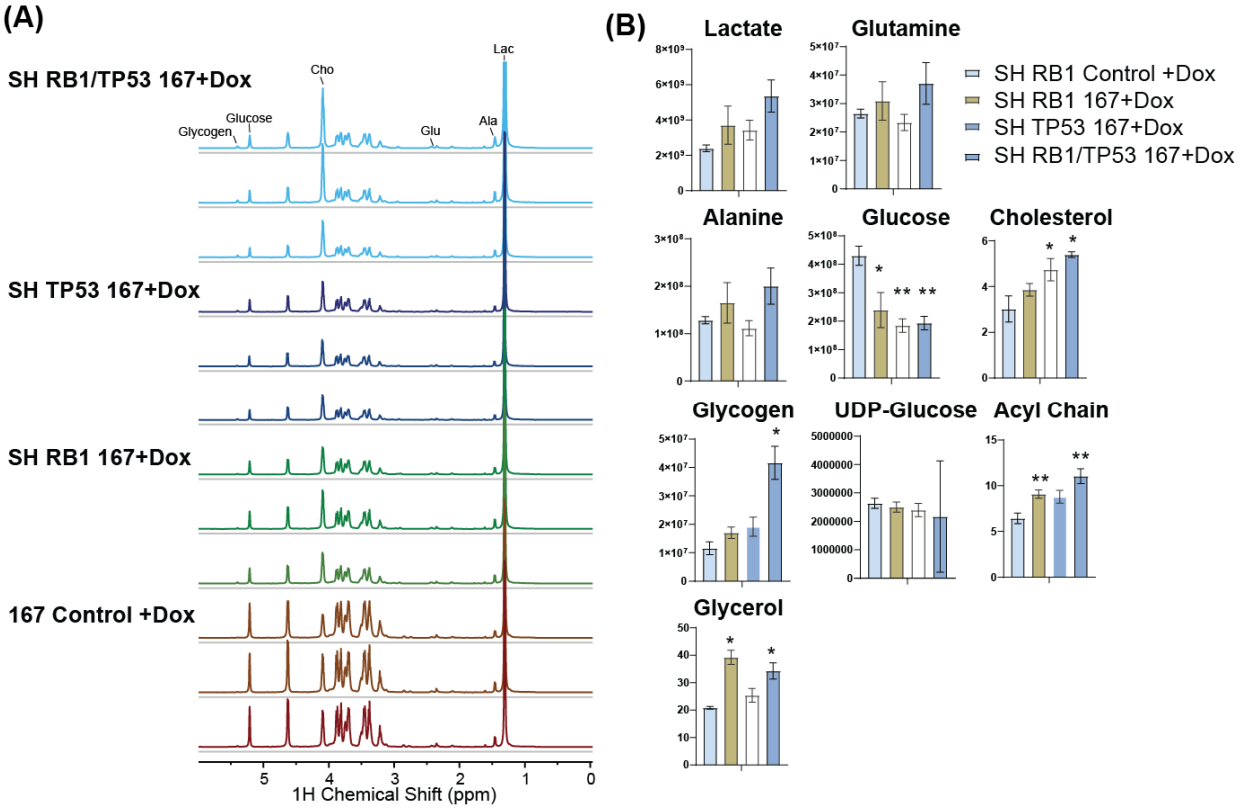


**Supplementary Figure 5. (A)** $^{1}$H-$^{13}$C HSQC NMR spectra of the polar fraction of 2 million LuCaP 167 organoid cells. Peaks used for assignment of specific metabolites are labeled by arrows **(B)** Quantification of metabolites from the polar and non-polar fractions. Multiplicity corrected p-values are calculated form two-way ANOVA test with Tukey's correction for multiple comparisons using Prism 9.0. p= * (0.05), ** (0.01), *** (0.001). Error bars indicate SD.

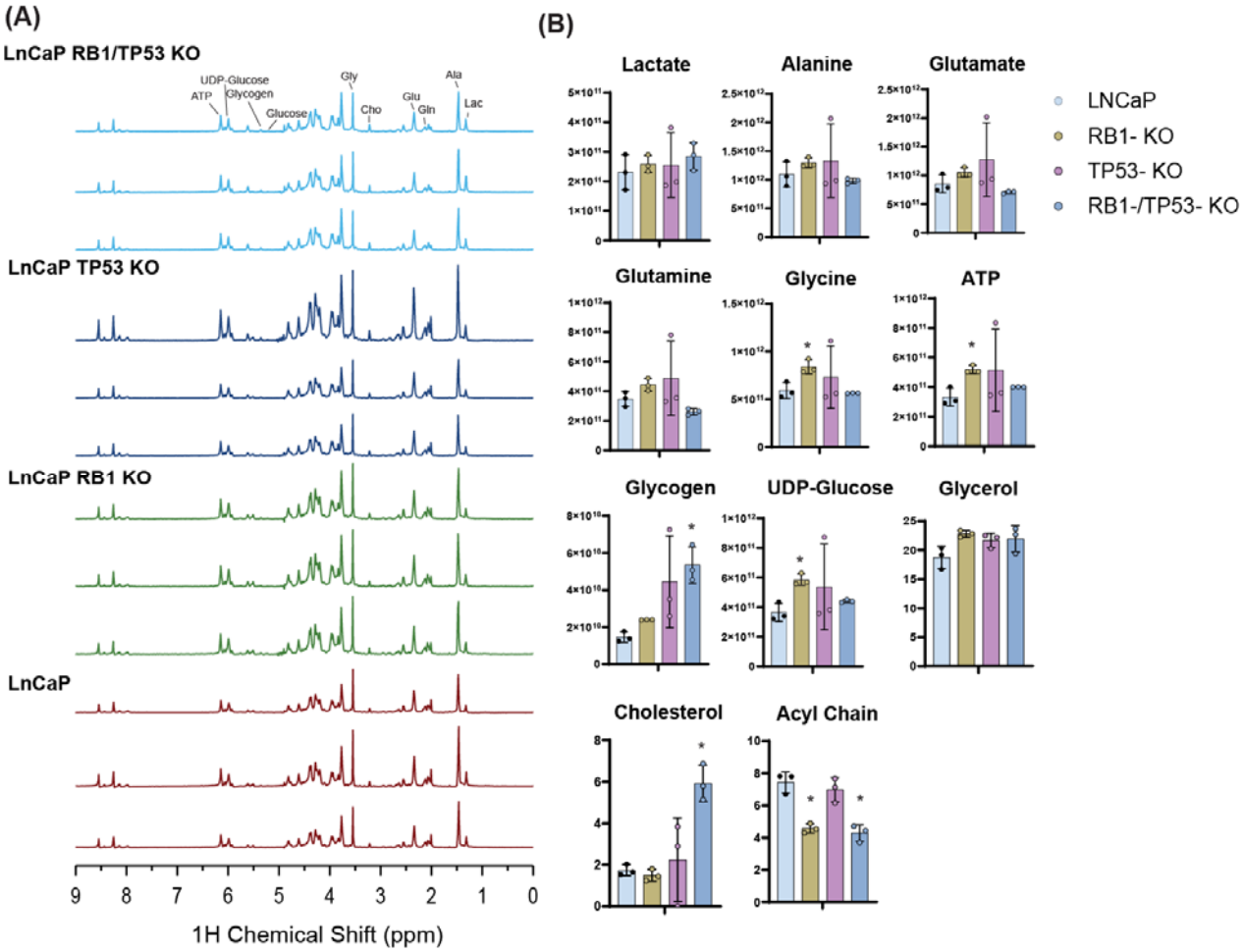


**Supplementary Figure 6. (A)** $^{1}$H-$^{13}$C HSQC NMR spectra of the polar fraction of LNCaP monoclonal Crispr KOs cells normalized to protein concentration by BCA. Peaks used for assignment of specific metabolites are labeled by arrows **(B)** Quantification of metabolites from the polar and non-polar fractions. Multiplicity corrected p-values are calculated form two-way ANOVA test with Tukey's correction for multiple comparisons using Prism 9.0. p= * (0.05), ** (0.01), *** (0.001). Error bars indicate SD.

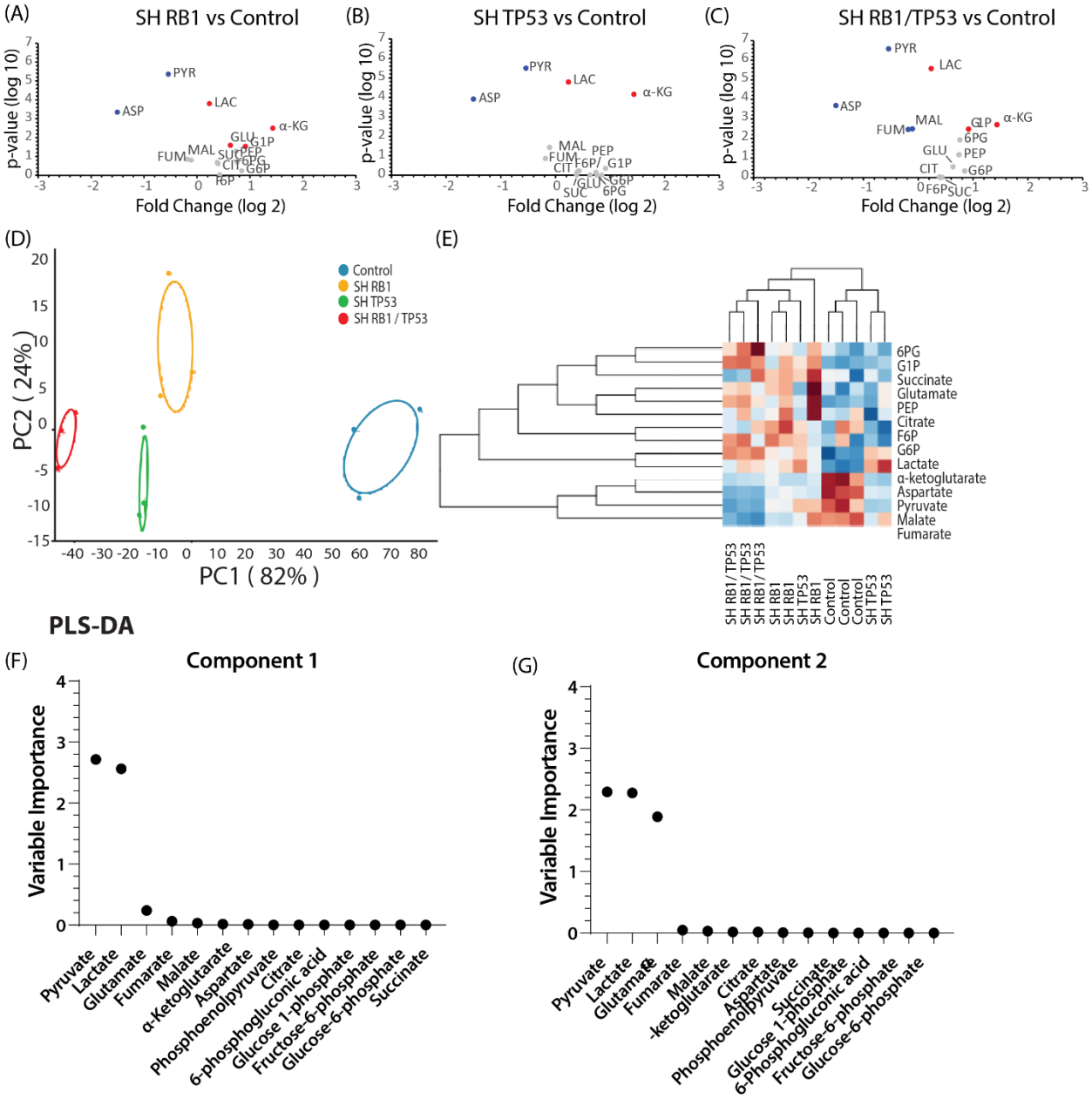


**Supplementary Figure 7. Metabolite concentrations from IC-MS of LuCaP 167 organoids with shRNA knockdown of *RB1* and/ or *TP53* relative to controls without shRNA. (A to C)** Volcano plot of the log 2-fold change versus the associated p-value. Blue is significantly upregulated; red is significantly upregulated with **(D)** Principal component plot of the normalized concentrations. The primary separation is the control samples from the RB1/TP53 depleted. **(E)** Heat map with hierarchal clustering **(F** and **G)** Variable importance for the first two components in a PLS-DA classification model for the four samples. The normalized concentrations of lactate, pyruvate, and fumarate are sufficient to separate the four samples ($R^2$=0.572).

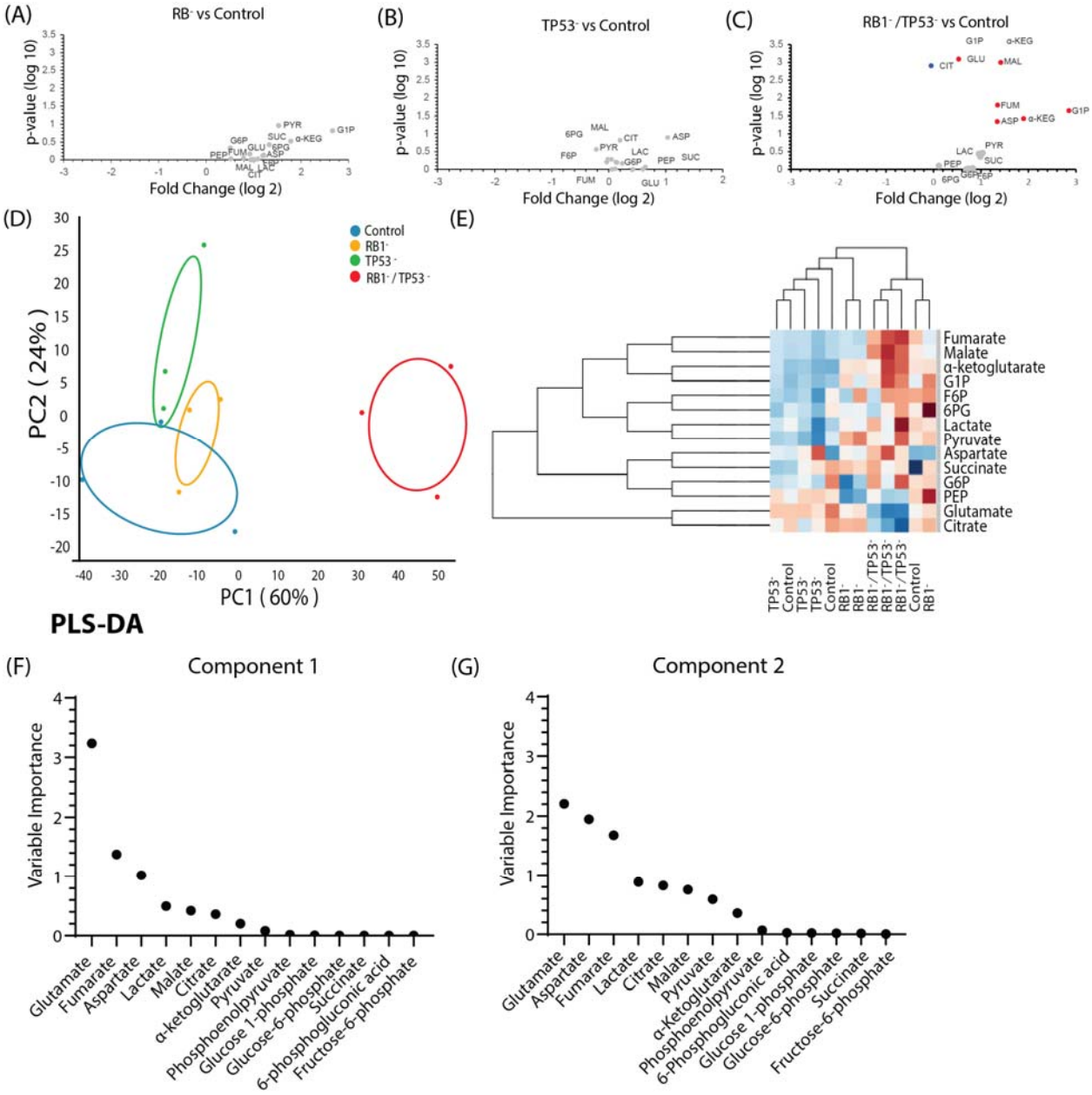


**Supplementary Figure 8. Metabolite concentrations from IC-MS of LnCaP monoclonal Crispr KO cells relative to control. (A to C)** Volcano plot of the log 2-fold change versus the associated p-value. Blue is significantly upregulated; red is significantly upregulated with **(D)** Principal component plot of the normalized concentrations. The primary separation is the RB1/TP53- dual knockout from the others. **(E)** Heat map with hierarchal clustering **(F and G)** Variable importance for the first two components in a PLS-DA classification model for the four samples. The metabolites in the TCA cycle primarily separate the samples.

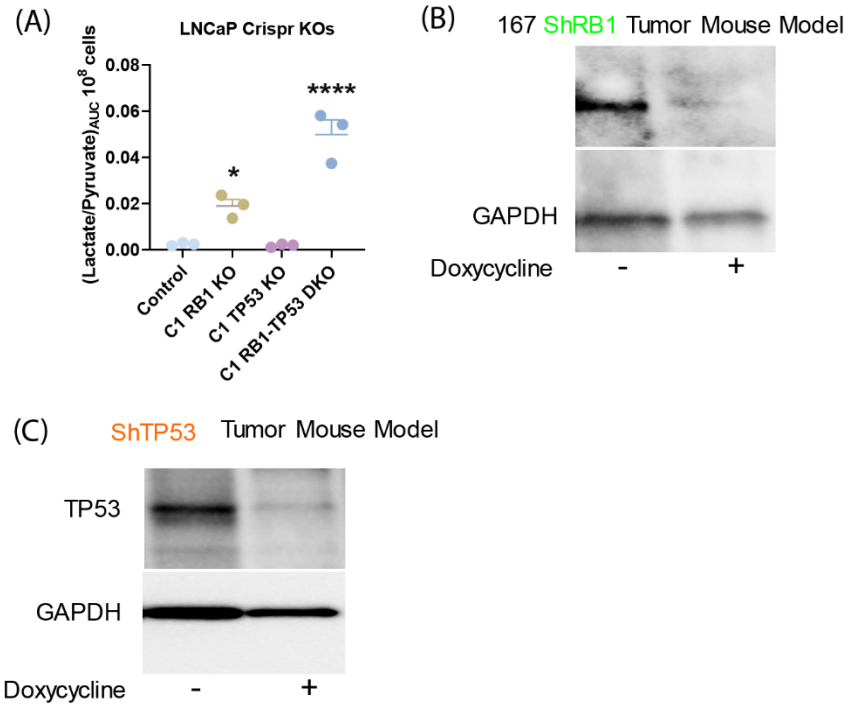


**Supplementary Figure 9. *RB1* alone or combined with *TP53* knockdown increases LDH flux detected *in vitro* by $^{13}$C-NMRS in LnCaP monoclonal Crispr Knockouts. (A)** Dot plot of the lactate/pyruvate conversion ratio for genetically modified *RB1* and/or *TP53* LNCaP Crispr knockout models in vitro. **(B and C)** Western blot of RB1 (B) and TP53 (C) protein levels in LuCaP167 organoid-derived PDX tumors with or without *in vivo* doxycycline induction of ShRNA as described in methods.

## References


**1.** Costello LC, Franklin RB. Aconitase activity, citrate oxidation, and zinc inhibition in rat ventral prostate. *Enzyme.* 1981;26:281-287.

**2.** Barron ESG, Huggins C. The Metabolism of Isolated Prostatic Tissue**This investigation was supported by a grant from the Committee for Research in Endocrinology, the National Research Council. *The Journal of Urology.* 1944;51:630-634.

**3.** Pertega-Gomes N, Felisbino S, Massie CE, et al. A glycolytic phenotype is associated with prostate cancer progression and aggressiveness: a role for monocarboxylate transporters as metabolic targets for therapy. *J Pathol.* 2015;236:517-530.

**4.** Massie CE, Lynch A, Ramos-Montoya A, et al. The androgen receptor fuels prostate cancer by regulating central metabolism and biosynthesis. *EMBO J.* 2011;30:2719-2733.

**5.** Shafi AA, Putluri V, Arnold JM, et al. Differential regulation of metabolic pathways by androgen receptor (AR) and its constitutively active splice variant, AR-V7, in prostate cancer cells. *Oncotarget.* 2015;6:31997-32012.

**6.** Sushentsev N, McLean MA, Warren AY, et al. Hyperpolarised (13)C-MRI identifies the emergence of a glycolytic cell population within intermediate-risk human prostate cancer. *Nat Commun.* 2022;13:466.

**7.** Watson PA, Arora VK, Sawyers CL. Emerging mechanisms of resistance to androgen receptor inhibitors in prostate cancer. *Nat Rev Cancer.* 2015;15:701-711.

**8.** Freedland SJ, Humphreys EB, Mangold LA, Eisenberger M, Dorey FJ, Walsh PC, Partin AW. Risk of Prostate Cancer–Specific Mortality Following Biochemical Recurrence After Radical Prostatectomy. *JAMA.* 2005;294:433-439.

**9.** Labrecque MP, Coleman IM, Brown LG, et al. Molecular profiling stratifies diverse phenotypes of treatment-refractory metastatic castration-resistant prostate cancer. *J Clin Invest.* 2019;129:4492-4505.

**10.** Quigley DA, Dang HX, Zhao SG, et al. Genomic Hallmarks and Structural Variation in Metastatic Prostate Cancer. *Cell.* 2018;174:758-769 e759.

**11.** Abida W, Cyrta J, Heller G, et al. Genomic correlates of clinical outcome in advanced prostate cancer. *Proc Natl Acad Sci U S A.* 2019;116:11428-11436.

**12.** Beltran H, Prandi D, Mosquera JM, et al. Divergent clonal evolution of castration-resistant neuroendocrine prostate cancer. *Nat Med.* 2016;22:298-305.

**13.** Sheng Yu Ku SR, Yanqing Wang, Ping Mu, Mukund Seshadri,, Zachary W. Goodrich MMG, David P. Labbé,, Eduardo Cortes Gomez JW, Henry W. Long, Bo Xu, Myles Brown,, Massimo Loda CLS, Leigh Ellis, David W. Goodrich. Rb1 and Trp53 cooperate to suppress prostate cancer lineage plasticity, metastasis, and antiandrogen resistance. *Science.* 2017;355:78-83.

**14.** Nyquist MD, Corella A, Coleman I, et al. Combined TP53 and RB1 Loss Promotes Prostate Cancer Resistance to a Spectrum of Therapeutics and Confers Vulnerability to Replication Stress. *Cell Rep.* 2020;31:107669.

**15.** Ping Mu ZZ, Matteo Benelli, Wouter R. Karthaus, Elizabeth Hoover,, Chi-Chao Chen JW, Sheng-Yu Ku, Dong Gao, Zhen Cao,, Neel Shah EJA, Wassim Abida, Philip A. Watson, Davide Prandi,, Chun-Hao Huang EdS, Scott W. Lowe, Leigh Ellis,, Himisha Beltran MAR, David W. Goodrich,, Francesca Demichelis CLS. SOX2 promotes lineage plasticity and antiandrogen resistance in TP53- and RB1-deficient prostate cancer. *Science.* 2017;355:84-88.

**16.** Mandigo AC, Yuan W, Xu K, et al. RB/E2F1 as a Master Regulator of Cancer Cell Metabolism in Advanced Disease. *Cancer Discov.* 2021;11:2334-2353.

**17.** Navone NM, van Weerden WM, Vessella RL, et al. Movember GAP1 PDX project: An international collection of serially transplantable prostate cancer patient-derived xenograft (PDX) models. *Prostate.* 2018;78:1262-1282.

**18.** Beshiri ML, Tice CM, Tran C, et al. A PDX/Organoid Biobank of Advanced Prostate Cancers Captures Genomic and Phenotypic Heterogeneity for Disease Modeling and Therapeutic Screening. *Clin Cancer Res.* 2018;24:4332-4345.

**19.** Iravani A, Violet J, Azad A, Hofman MS. Lutetium-177 prostate-specific membrane antigen (PSMA) theranostics: practical nuances and intricacies. *Prostate Cancer Prostatic Dis.* 2020;23:38-52.

**20.** Qiu X, Boufaied N, Hallal T, et al. MYC drives aggressive prostate cancer by disrupting transcriptional pause release at androgen receptor targets. *Nat Commun.* 2022;13:2559.

**21.** Sowalsky AG, Figueiredo I, Lis RT, et al. Assessment of Androgen Receptor Splice Variant-7 as a Biomarker of Clinical Response in Castration-Sensitive Prostate Cancer. *Clin Cancer Res.* 2022;28:3509-3525.

**22.** Reinfeld BI, Madden MZ, Wolf MM, et al. Cell-programmed nutrient partitioning in the tumour microenvironment. *Nature.* 2021;593:282-288.

**23.** Nguyen HM, Vessella RL, Morrissey C, et al. LuCaP Prostate Cancer Patient-Derived Xenografts Reflect the Molecular Heterogeneity of Advanced Disease an--d Serve as Models for Evaluating Cancer Therapeutics. *Prostate.* 2017;77:654-671.

**24.** Tanner LB, Goglia AG, Wei MH, et al. Four Key Steps Control Glycolytic Flux in Mammalian Cells. *Cell Syst.* 2018;7:49-62 e48.

**25.** Bluemn EG, Coleman IM, Lucas JM, et al. Androgen Receptor Pathway-Independent Prostate Cancer Is Sustained through FGF Signaling. *Cancer Cell.* 2017;32:474-489 e476.

**26.** Buteau JP, Martin AJ, Emmett L, et al. PSMA and FDG-PET as predictive and prognostic biomarkers in patients given [(177)Lu]Lu-PSMA-617 versus cabazitaxel for metastatic castration-resistant prostate cancer (TheraP): a biomarker analysis from a randomised, open-label, phase 2 trial. *Lancet Oncol.* 2022;23:1389-1397.

**27.** Eshghi A, Covington MF, Eshghi N, Kuo PH. Utility of PET to Appropriately Select Patients for PSMA-Targeted Theranostics. *Clin Nucl Med.* 2022;47:488-495.

**28.** Seifert R, Telli T, Hadaschik B, Fendler WP, Kuo PH, Herrmann K. Is (18)F-FDG PET Needed to Assess (177)Lu-PSMA Therapy Eligibility? A VISION-like, Single-Center Analysis. *J Nucl Med.* 2023;64:731-737.

**29.** Jadvar H. The VISION Forward: Recognition and Implication of PSMA-/(18)F-FDG+ mCRPC. *J Nucl Med.* 2022;63:812-815.

**30.** Bok R, Lee J, Sriram R, et al. The Role of Lactate Metabolism in Prostate Cancer Progression and Metastases Revealed by Dual-Agent Hyperpolarized (13)C MRSI. *Cancers (Basel).* 2019;11.

**31.** Certo M, Tsai CH, Pucino V, Ho PC, Mauro C. Lactate modulation of immune responses in inflammatory versus tumour microenvironments. *Nat Rev Immunol.* 2021;21:151-161.

**32.** Drost J, Karthaus WR, Gao D, Driehuis E, Sawyers CL, Chen Y, Clevers H. Organoid culture systems for prostate epithelial and cancer tissue. *Nat Protoc.* 2016;11:347-358.

**33.** Adelaiye-Ogala R, Gryder BE, Nguyen YTM, et al. Targeting the PI3K/AKT Pathway Overcomes Enzalutamide Resistance by Inhibiting Induction of the Glucocorticoid Receptor. *Mol Cancer Ther.* 2020;19:1436-1447.

**34.** Crooks DR, Fan TW, Linehan WM. Metabolic Labeling of Cultured Mammalian Cells for Stable Isotope-Resolved Metabolomics: Practical Aspects of Tissue Culture and Sample Extraction. *Methods Mol Biol.* 2019;1928:1-27.

**35.** Palmer AG, Cavanagh J, Wright PE, Rance M. Sensitivity improvement in proton-detected two-dimensional heteronuclear correlation NMR spectroscopy. *Journal of Magnetic Resonance (1969).* 1991;93:151-170.

**36.** Fan TW, Lane AN. Applications of NMR spectroscopy to systems biochemistry. *Prog Nucl Magn Reson Spectrosc.* 2016;92-93:18-53.

**37.** Sun Q, Fan TW, Lane AN, Higashi RM. An Ion Chromatography-Ultrahigh-Resolution-MS(1)/Data-Independent High-Resolution MS(2) Method for Stable Isotope-Resolved Metabolomics Reconstruction of Central Metabolic Networks. *Anal Chem.* 2021;93:2749-2757.

**38.** Crooks DR, Maio N, Lane AN, et al. Acute loss of iron-sulfur clusters results in metabolic reprogramming and generation of lipid droplets in mammalian cells. *J Biol Chem.* 2018;293:8297-8311.

**39.** Lin P, Dai L, Crooks DR, et al. NMR Methods for Determining Lipid Turnover via Stable Isotope Resolved Metabolomics. *Metabolites.* 2021;11.

**40.** Yamamoto K, Brender JR, Seki T, et al. Molecular Imaging of the Tumor Microenvironment Reveals the Relationship between Tumor Oxygenation, Glucose Uptake, and Glycolysis in Pancreatic Ductal Adenocarcinoma. *Cancer Res.* 2020;80:2087-2093.